Journal of Neuroscience Methods 235 (2014) 316–330

Contents lists available at ScienceDirect

Journal of Neuroscience Methods

journal homepage: www.elsevier.com/locate/jneumeth

Computational Neuroscience

On the robustness of EC–PC spike detection method for online neural recording

Yin Zhou[a,b], Tong Wu[a], Amir Rastegarnia[c], Cuntai Guan[d], Edward Keefer[e], Zhi Yang[a,*]

[a] Department of Electrical and Computer Engineering, National University of Singapore, 117583 Singapore, Singapore
[b] Institute of VLSI Design, Zhejiang University, Hangzhou 310027, China
[c] Department of Electrical Engineering, Malayer University, Malayer 95863-65719, Iran
[d] Department of Neural and Biomedical Technology, Institute for Infocomm Research, A*STAR, 138632 Singapore, Singapore
[e] Nerves Incorporated, Dallas, TX 75206, USA

HIGHLIGHTS

- We evaluate the performance of EC–PC spike detection method under different firing rates, SNRs.
- Both simulated and experimental data are used in the performance evaluations.
- Results show that the EC–PC detection method is the most robust in comparison with some popular detectors.
- We show that the detection Precision can be derived without requiring additional user input parameters.
- We also report a hardware implementation based on a 0.13 μm CMOS chip.

ARTICLE INFO

Article history:
Received 18 November 2013
Received in revised form 9 July 2014
Accepted 10 July 2014
Available online 1 August 2014

Keywords:
Spike detection
Precision of detection
EC–PC
ASIC implementation

ABSTRACT

Background: Online spike detection is an important step to compress neural data and perform real-time neural information decoding. An unsupervised, automatic, yet robust signal processing is strongly desired, thus it can support a wide range of applications. We have developed a novel spike detection algorithm called "exponential component–polynomial component" (EC–PC) spike detection.
New method: We firstly evaluate the robustness of the EC–PC spike detector under different firing rates and SNRs. Secondly, we show that the detection Precision can be quantitatively derived without requiring additional user input parameters. We have realized the algorithm (including training) into a 0.13 μm CMOS chip, where an unsupervised, nonparametric operation has been demonstrated.
Results: Both simulated data and real data are used to evaluate the method under different firing rates (FRs), SNRs. The results show that the EC–PC spike detector is the most robust in comparison with some popular detectors. Moreover, the EC–PC detector can track changes in the background noise due to the ability to re-estimate the neural data distribution.
Comparison with existing methods: Both real and synthesized data have been used for testing the proposed algorithm in comparison with other methods, including the absolute thresholding detector (AT), median absolute deviation detector (MAD), nonlinear energy operator detector (NEO), and continuous wavelet detector (CWD). Comparative testing results reveals that the EP–PC detection algorithm performs better than the other algorithms regardless of recording conditions.
Conclusion: The EC–PC spike detector can be considered as an unsupervised and robust online spike detection. It is also suitable for hardware implementation.

1. Introduction

Neurons in the brain form closely connected networks and use action potentials to transfer information (Gerstner et al., 1997; Buzsaki, 2006). To study information generation, representation and propagation, action potentials need to be extracted from the raw data, a process known as spike detection (Lewicki, 1998).

* Corresponding author.
E-mail address: eleyangz@nus.edu.sg (Z. Yang).

http://dx.doi.org/10.1016/j.jneumeth.2014.07.006
0165-0270/

So far different spike detection algorithms have been reported in the literature (Chandra and Optican, 1997; Harrison, 2003; Gibson et al., 2009; Quiroga et al., 2004; Kim and Kim, 2000, 2003; Mukhopadhyay and Ray, 1998; Choi et al., 2006; Semmaoui et al., 2012; Gosselin and Sawan, 2009; Maragos et al., 1993; Goodall and Horch, 1992; Mtetwa and Smith, 2006; Kaneko et al., 1999; Gozani and Miller, 1994; Kim and McNames, 2007; Harris et al., 2000; Henze et al., 2000; Zouridakis and Tam, 1997; Nenadic and Burdick, 2005). In the methods that rely on amplitude thresholding (Chandra and Optican, 1997; Harrison, 2003), spikes are detected when neural data exceed a pre-determined threshold, usually 3–6 times the root mean squared (RMS) value of the data. Because of the computational simplicity, the amplitude thresholding detection is suitable for on-line implementation (Gibson et al., 2009; Quiroga et al., 2004). However, its performance is not reliable at moderate or low SNRs conditions. The other candidates for on-line implementation are the nonlinear energy operator (NEO) based methods (Kim and Kim, 2000; Mukhopadhyay and Ray, 1998; Choi et al., 2006; Semmaoui et al., 2012; Gosselin and Sawan, 2009). In these methods, both instantaneous amplitude and frequency are taken into account to improve the detection accuracy. However, these methods provide satisfactory results only when the background noise can be described according to the undamped oscillator model (Maragos et al., 1993), which may not be valid in many situations. Another popular spike detection method is template matching, where spikes are detected according to the similarity between neural data and candidate spike template (Goodall and Horch, 1992; Mtetwa and Smith, 2006; Kaneko et al., 1999; Gozani and Miller, 1994; Kim and McNames, 2007). It is effective given appropriately trained templates and stable neural signals; however, neural spikes may have both short-term and long-term variations that can cause false detection (Harris et al., 2000; Henze et al., 2000). In addition, cross-bin similarity measure and globally searching for the best match can be slow (Kim and McNames, 2007). Wavelet-based detectors are also used in spike detection (Kim and Kim, 2003; Zouridakis and Tam, 1997; Nenadic and Burdick, 2005). Similar to template matching, they require well-shaped mother wavelets to form suboptimal matched filters (Shalchyan et al., 2012). This approach requires the user to specify threshold at each individual layer followed by a joint decision making mechanism. Also the algorithm requires a considerable amount of computation for implementation (Nenadic and Burdick, 2005).

In our previous work (Yang et al., 2012), a new EC–PC framework for in vivo spike detection has been proposed. It is shown that neural data are a combination of two components including noise and detectable spikes. After Hilbert transform, the noise forms an exponential component (EC) and spikes form a polynomial component (PC). By using online trained EC and PC from raw data, the detector can output a probability map for spike detection. In this paper, we briefly introduce the EC–PC detection method, and evaluate its performance under different conditions (firing rates, SNRs), and in comparison with other methods. Both simulated and experimental data are used in the performance evaluations, showing that the EC–PC detection method is the most robust in comparison with some popular detectors.

However, the main contribution of this paper is to show that regardless of the recording condition, the numeric value of the probability threshold of the EC–PC detector is approximately equal to the expectation of *detection Precision*. In other words, we prove theoretically that the detection Precision can be quantitatively derived without requiring additional user input parameters. This new feature allows directly mapping a detection threshold to a point on the probability of false alarm (PFA) curve. As a result, the user can pick operation points from the receiver operating characteristic (ROC) curve, and the algorithm will automatically adjust the threshold accordingly. We also report a hardware implementation based on a 0.13 μm Complementary Metal Oxide Semiconductor (CMOS) chip, where an unsupervised, nonparametric operation has been demonstrated. The chip takes 2.5 s for training from the raw data (not requiring any user specified parameter), where once trained a real-time performance has been obtained.

The rest of this paper is organized as follows. Section 2 gives the algorithm formulation. Section 3 describes data preparations and testing protocols. Experimental results are presented in Section 4. Algorithm implementation in ASIC and testing results are summarized in Section 5. Discussions and concluding remarks are given in Section 6.

2. Robustness of the EC–PC detection algorithm

2.1. Algorithm overview

Extracellularly recorded neural data consist of neural spikes (300 Hz–5 kHz), field potentials (<250 Hz, Belitski et al., 2008), and noise. After applying highpass filtering on the raw neural data at 300 Hz, the filtered signal contains the following components

1. Activities of neurons within the recording radius, where spike power is much stronger than the noise power.
2. Activities of neurons in an extended radius (up to a few hundred μm), where spike power is comparable to the noise power.
3. Noise produced by different sources including unresolved synaptic activities, firing of distant neurons, and recording hardware.

To examine the recorded neural data distribution, let denote by $V(t)$ and $HV(t)$ the neural data sequence and its Hilbert transform respectively.[1] They together form a strong analytic signal as

$$V_{st}(t) = V(t) + jHV(t) = V(t) + j\frac{1}{\pi}\beta\int_{-\infty}^{\infty}\frac{V(\tau)}{t-\tau}\,d\tau \quad (1)$$

where $j^2 = -1$ and β in front of the integral denotes the Cauchy principal value. The instantaneous power of the analytic signal $V_{st}(t)$, is then given by

$$Z(t) = |V_{st}(t)|^2 \quad (2)$$

It is shown in Yang et al. (2012) that for recordings with less visually detectable spikes, the probability density function of $Z(t)$ (denoted by $f(Z)$) is an exponential function as

$$f(Z) \approx f_n(Z) \approx \frac{1}{2\sigma^2}e^{-(Z/2\sigma^2)}, \quad Z \geq 0 \quad (3)$$

where $f_n(Z)$ denotes the probability density function of noise term and σ is the data standard deviation. For moderate and high SNR recordings, the tale of $f(Z)$ is mainly contributed from spikes and follows a polynomial function as (see Appendix A for more details)

$$f(Z) \approx f_d(Z) \approx Z^{-((3+2x)/2x)} \quad (4)$$

where x is real number within 1–2. Both expressions in (3) and (4) together suggest that $f(Z)$ is a combination of an exponential component (EC, $e^{-\lambda_1 Z}$, generated by noise) and a polynomial component (PC, $Z^{-\lambda_2}$, generated by spikes), as illustrated in Fig. 1.

Now, let assume that $\tilde{f}_n(Z)$ and $\tilde{f}_d(Z)$ are the exponential component and the polynomial component, trained in real-time respectively. Then, the *spiking probability*, i.e. the probability that

[1] The Hilbert transform is used for two reasons. First, extracellular spike could have significant variation in shape. In comparison with data sequence, the corresponding analytic signal has less variation in shape and only require a single threshold for different shaped spikes. Second, as to be derived here, background noise has a simple representation in Hilbert space.

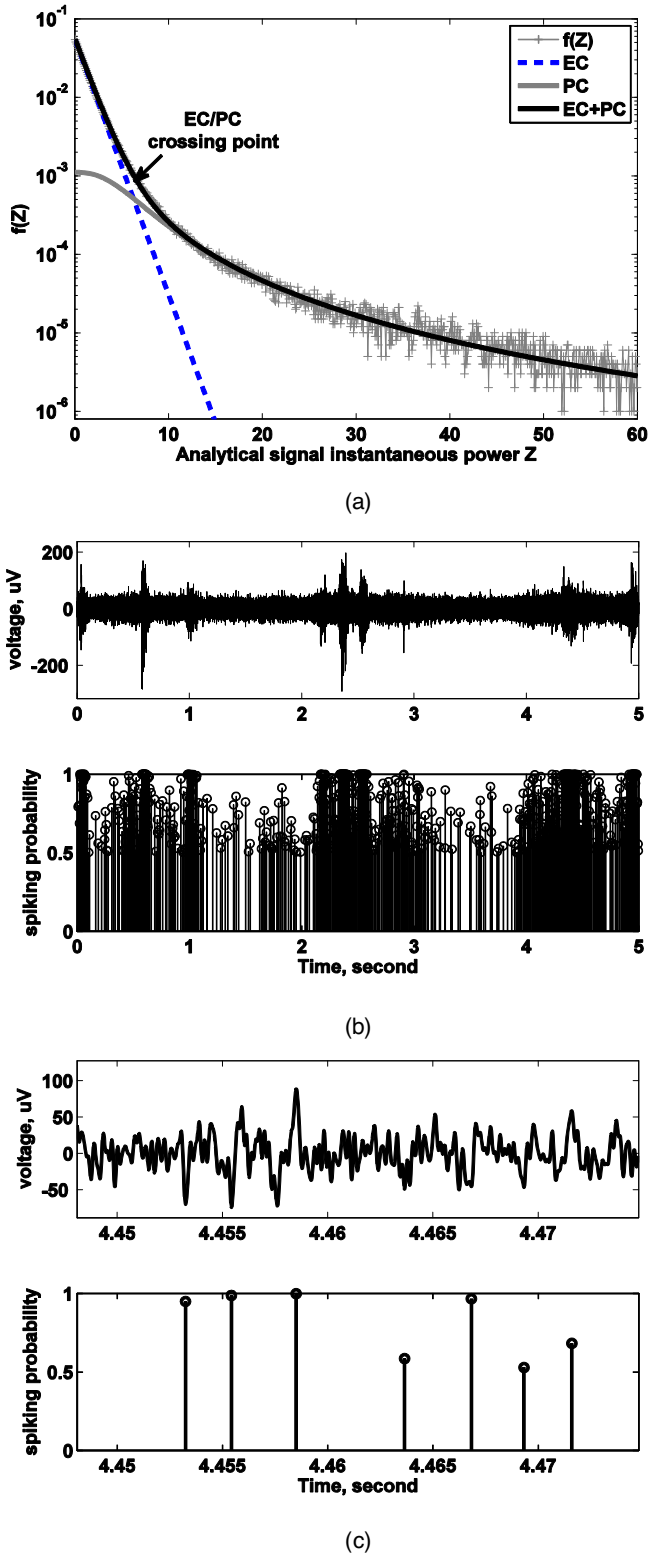

Fig. 1. EC–PC decomposition (the figure is adopted from Yang et al., 2012). (a) *X*-Axis is the analytical signal power normalized to data variance and *Y*-axis is pdf. The figure shows the estimated EC (dashed blue), PC (solid gray) and superimposed EC + PC (solid black) in comparison with neural data distribution ($f(Z)$, dotted gray). (b) Spiking probability map of a 5 s in vivo data. Upper, bandpass filtered neural data. Bottom, corresponding spiking probability map with probabilities greater than 0.5 are plotted. *X*-Axis is time and *Y*-axis the spiking probability. (c) Zoom-in figure at around 4.46 s. (For interpretation of the references to color in this figure legend, the reader is referred to the web version of the article.)

a data point with instantaneous power Z is from a spike, can be quantitatively assessed by

$$p(Z) = \frac{\tilde{f}_d(Z)}{\tilde{f}_d(Z) + \tilde{f}_n(Z)} \approx \frac{(b/(Z^{\lambda_2} + c))}{(b/Z^{\lambda_2} + c) + ae^{-\lambda_1 Z}} \tag{5}$$

where $\{a, b\}$ are the normalization coefficients that make $f(Z)$ sum to one and c is added to regulate PC to avoid $f(Z)$ from going infinite at small values of Z. Specially, the data point Z satisfying $p(Z) = 0.5$ is defined as EC–PC crossing point, at which point spike power is equal to noise power and EC and PC curves in Fig. 1 cross each other. The square root of crossing point is denoted by $Z^{0.5}_{EC/PC}$. When a sequence has large number of spikes, PC curve moves upwards, which in turn leads to a small $Z^{0.5}_{EC/PC}$. Let $[m_i \Delta T, m_{i+1} \Delta T]$ be an arbitrary time window of a few ms, where $m = \ldots, -1, 0, 1, 2, \ldots$ and ΔT is the sampling interval. If we adopt a winner-take-all strategy, the probability that at least one spike appears in the ith window can be approximated by the peak spiking probability of the data points in the window as

$$P(i) = p(Z_i), \quad Z_i = \max\{Z(m\Delta T)\}, \quad m_i \le m < m_{i+1} \tag{6}$$

A plotting of $P(i)$ over time is a predictive map of spikes and defined as *spiking probability map*, which is illustrated in Fig. 1(b) and (c). Spike detection can be then performed by applying threshold on the spiking probability map.

2.2. Spiking probability

As mentioned above, the noise exhibits an exponential component and the spikes exhibit a polynomial component in the data distribution. Knowing these two distributions, a probability value is then assigned to every detected spike, which varies from '0' to '1' with '0' corresponds to 'definitely not a spike' and '1' corresponds to 'definitely a spike'. The threshold applied to the spiking probability map is thus a *probability threshold*, which is denoted as P_{TH}. Let define the Precision of the detection (Fawcett, 2006), also used in Section 2.3.1, as

$$\text{Precision} = \frac{N_{cd}}{N_d} \tag{7}$$

where N_{cd} is the number of correctly detected spikes and N_d is the number of total detected spikes. Now, we claim the following proposition.

Theorem 1. *The Precision of the detection in (7) can be directly predicted by the probability threshold P_{TH}, by the following relationship*

$$\text{Precision} \approx \frac{N_{cd}}{N_{cd} + \alpha N_{fd}} = P_{TH} \tag{8}$$

where α is the parameter left to quantify the relative contribution from false spikes.

Proof. See Appendix B. □

Our analysis suggests that the color of background noise influences the value of α and in general, α is close to one. To examine the statistics of α, neural noise of different spectrum characteristics were used in simulated data. For each noise trial, 121 sequences with total firing rate ranging from 15 Hz to 90 Hz and SNR ranging from 3 to 5 have been synthesized. The data simulation protocol follows in Section 3.1.1.

3. Database and protocol

This section introduces the database and protocol which has been used in the paper.

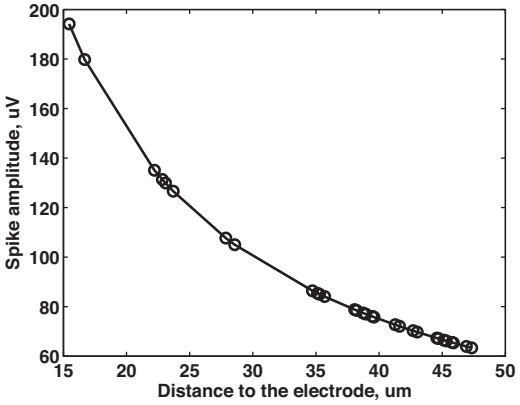

Fig. 2. Spike template voltage vs. neuron to electrode distance. Neuron spacing equals to 25 μm, $A = 120$ μV and $x = 1$. Each dot indicates one neuron and total 30 neurons are plotted.

3.1. Database

3.1.1. Simulated data

The simulated data are constructed by scaling and adding spikes into noisy segment. Recorded in vivo data that do not contain visually detectable spikes are used as the background noise (20–30 μV RMS). The extracted spike waveforms with large amplitude (>300 μV) are used as spike templates. The traditional protocols used for generating simulated data assume only one spike template in the noise sequence, while in our data synthesis protocol, we have considered a more realistic case. To be more precise, when an electrode is inserted into the brain, it is surrounded by a large number of neurons. Those located close to the electrode generate large spikes in the recording data and those far from the electrode generate small spikes. Thus, the amplitude of each template V_M is scaled according to the distance between the electrode and space location of corresponding neuron (see Eq. (10)).

The scaling of the spike templates is based on the assumptions that first neurons are uniformly distributed in the space where the origin (0, 0, 0) represents the location of the electrode; second the amplitude of the spikes decrease as $1/r^x$ where r is the distance between neurons and electrode and x is a factor within 1 and 2. The data synthesis steps are

1. Place 64 neurons to form a cubic lattice structure centered at the origin and the space between the neighbor neurons is normalized to be one.
2. Randomly locate the electrode in a small region around the origin (within (±0.25,±0.25,±0.25)) to generate different scaling factors and avoid unreasonably large spikes.
3. Choose 30 neurons that are most close to the electrode.
4. Get the scaling factors for these neurons as $V_M = A/r^x$. For unit normalized distance, A could choose around 100 μV. In the real data, the neuron density is around 50,000–100,000 per mm^3 which means 20–30 μm for one normalized space. A typical distance versus amplitude curve is given in Fig. 2 with neurons denoted as dots. The x-axis can be scaled depending on the neuron density and more neurons can be included by further extending the recording range to more than 100 μm. However, because of the limited number of spike templates and to avoid small spikes which are more likely to be below the noise level (20 μV in RMS) we choose 30 neurons in our simulated data set.

The sampling frequencies of the spike templates and the simulated data are both 40 kHz. There are 120 templates in our spike template bank. They have different shape (positive peak, negative peak and having both positive and negative peaks) and different width from more than 2 ms to less than 1 ms (see Fig. 12(a)). The value of x in Eq. (10) is randomly set between 1 and 2. In the experiments, we used 30 neurons (thus 30 templates) and keep the total firing rate of one data sequence below 100 Hz. Individual neurons' firings are assumed to follow Poisson process. The SNR in our experiments is defined as the averaged peak amplitude of spike templates over background noise RMS

$$\mathrm{SNR} = \frac{(1/n)\sum_{i=1}^{n} |V_i|}{\mathrm{RMS}_n}$$

where V_i is peak amplitude of each spike template and RMS_n is noise RMS value. We have built simulated datasets with different SNR and firing rates to test the detection performance of EC–PC detector.

3.1.2. Simultaneous intracellular recording data

Another way for quantitative assessment of the spike detection algorithm is to use simultaneous intracellular recording data which are available from a public database contributed by Buzsaki's Lab (Harris et al., 2000; Henze et al., 2000). The advantage of simultaneous intracellular recording is that it records neuron's intracellular signals which are large in magnitude and can be viewed as ground truth and at the same time it records extracellular data with multichannel electrodes located outside of neurons. The use of simultaneous intracellular recording for performance evaluation is not straightforward. The electrode located close to the soma could have large intra-labeled spikes (the extracellular spikes indicated by intracellular recorded signal) and these spikes can be easily detected by many detectors. Electrodes far from the soma may miss intra-labeled spikes which become totally submerged in the noise, but record large amplitude spikes from other more proximally located neurons. In Shahid et al. (2010) the authors directly use the simultaneous recorded data treating the spikes from other neurons as false positives and comparing the detector performance by carefully sweeping threshold then counting the number of true positives, false negatives and false positives. It biases the performance when large spikes from other neurons exist. The method given in Obeid (2007) pre-detects these spikes as from a "secondary neuron" and count them neither as true positives nor as false positives. It avoids the influence from other neurons however the performance evaluation is biased by the pre-detector.

In this work, we pick the simultaneous recording data from high spiking probability channels (averaged spiking probabilities of intra-labeled spikes larger than 0.99), and extract every intra-labeled spike waveforms and their precise spike timing. Then we pick data from low spiking probability channels (few visually detectable spikes) as background noise. After scaling and adding together the background noise and the spike signals, we get new data with the ground truth from more than one neuron. The advantage of this data preparation protocol is twofold. First, it captures the actual spike timing and spike waveform deviation from in vivo recordings while maintains the controllable SNR and the rejection of large spikes from unlabeled neurons. Second, it is similar to those used in the most reference papers (Choi et al., 2006; Nenadic and Burdick, 2005) that use small number of neurons and do not consider amplitude scaling as a function of neuron-electrode distance. Here we use spike signals from three simultaneous intracellular recording sequences and the generated data are shown in Fig. 3. Neuron 1 has high firing rate (>5 Hz), neuron 2 has low firing rate (<1 Hz) while neuron 3 bursts thus has large spike amplitude deviation. Note that in Fig. 3, the scale of y-axis is without any unit. First we normalized the noise sequence to make its RMS value to be one. Then we scaled all the sequences to get the wanted SNR which is 4

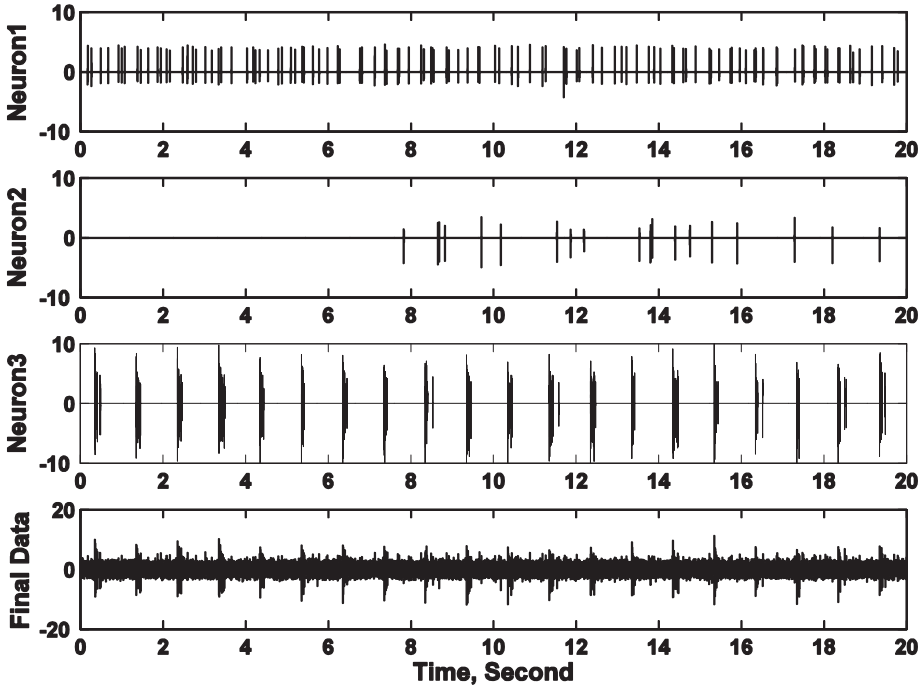

Fig. 3. The top panel is the first neuron extracted from dataset d16613.001, channel 2, 50–70 s, containing 112 spikes. The second panel is extracted from dataset d16311.002, channel 3, 50–70 s, containing 19 spikes. The third panel is extracted from dataset d18711.003, channel 5, 50–70 s, containing 170 spikes. The bottom panel is the final data obtained from adding together neuron 1, neuron 2, neuron 3 and noise segment from dataset d16311.001, channel 8, 50–70 s. The choice of 20 s data is arbitrary. In this figure, spike amplitudes and noise RMS are scaled to make SNR = 4.

in this figure. In real data, the averaged spike amplitude for neuron 1, 2 and 3 is 460 μV, 460 μV and 160 μV respectively.

3.1.3. Real data from anesthetized rat

To support the proposed work as a candidate of robust spike detector, we have designed a controlled experiment on an anesthetized rat: a pair of microelectrodes is navigated into rat's brain to identify a recording location that gives sustained brain activities. After fixing the recording location, an anesthesia drug is injected to gradually stop the animal heart beating. As a result, neurons are dying because of lack of fresh blood. 80 min neural recordings at 25 kHz/16b start from the electrode placement and last till the end of rat's life (data RMS reach a floor of around 10 μV). Although we do not know the exact firing pattern of individual neurons, it is obvious that the firing rate estimated from the spike detection result should be decreased with time.

3.2. Testing experiments

3.2.1. Experiment using simulated data – ROC curves

ROC curves (Fawcett, 2006) are widely used for detection performance evaluation. In this experiment, we compare the ROC curves of different methods including the proposed EC–PC detection method, CWD, AT with RMS estimator, AT with median absolute deviation estimator (MAD) and NEO. The threshold of NEO is chosen as several times of the mean of NEO output as used in Gibson et al. (2010). The ROC comparison is performed under 9 different SNR/Firing rate situations and for each situation, the ROC curves are generated by averaging the results from 100 random trials.

Another reason why we use ROC curves is that we can select "optimal thresholds" for each detector to fairly compare their robustness in the following experiments. The threshold is actually a trade-off between true detections and false alarms. An optimal threshold only exists in high SNR recordings where most of the spikes can be successfully detected with few false alarms. This leads to a "turning point" in ROC curves where the curves start to be close to one. However, the optimal threshold does not always exist because in most cases the "turning point" cannot be clearly observed. It is further added that even one threshold is learned to be optimal in one sequence, it is often not optimal in another. To fairly compare the robustness of each spike detector, we selected the "reasonable thresholds" using the similar idea from Gibson et al. (2010). When forming the ROC curves, those thresholds which cause reasonable detection results (the probability of detection (PD) >0.7 and probability of false alarms (PFA) <0.3) were recorded. Since the total 900 simulation data cover a wide range of SNRs and firing rates, the reasonable thresholds of each detector were selected and further used in our experiments such that they gave the largest number of reasonable detection results. From the ROC curves, the selected thresholds for each detector are EC–PC = 0.8, CWD = −0.1, AT = 3.5× data RMS, MAD = 4×STD, NEO = 10 which will be used in the following experiments.

3.2.2. Experiment using simultaneous recording data – SNR changes

We first performed EC–PC spike detection on simultaneous intracellular recording data as described in Section 3.1.2. The SNR levels of the data were set to be 3–6. Several metrics were listed to show the performance: P (actual positive, true spikes added in the sequence), TP (true positive, correctly detected spikes), FP (false positive, falsely detected spikes), FN (false negative, true spikes that are not detected by the detector), SE (sensitivity, defined as TP/P) and PR (Precision, defined as TP/(TP + FP)). The experiments were repeated 100 times to get statistical results by randomly adding noise segments under different SNRs.

3.2.3. Experiment using simulated data – FR changes

Simulated data were used to quantitatively study the robustness of the detectors to the situation where spike firing rate (FR) keeps

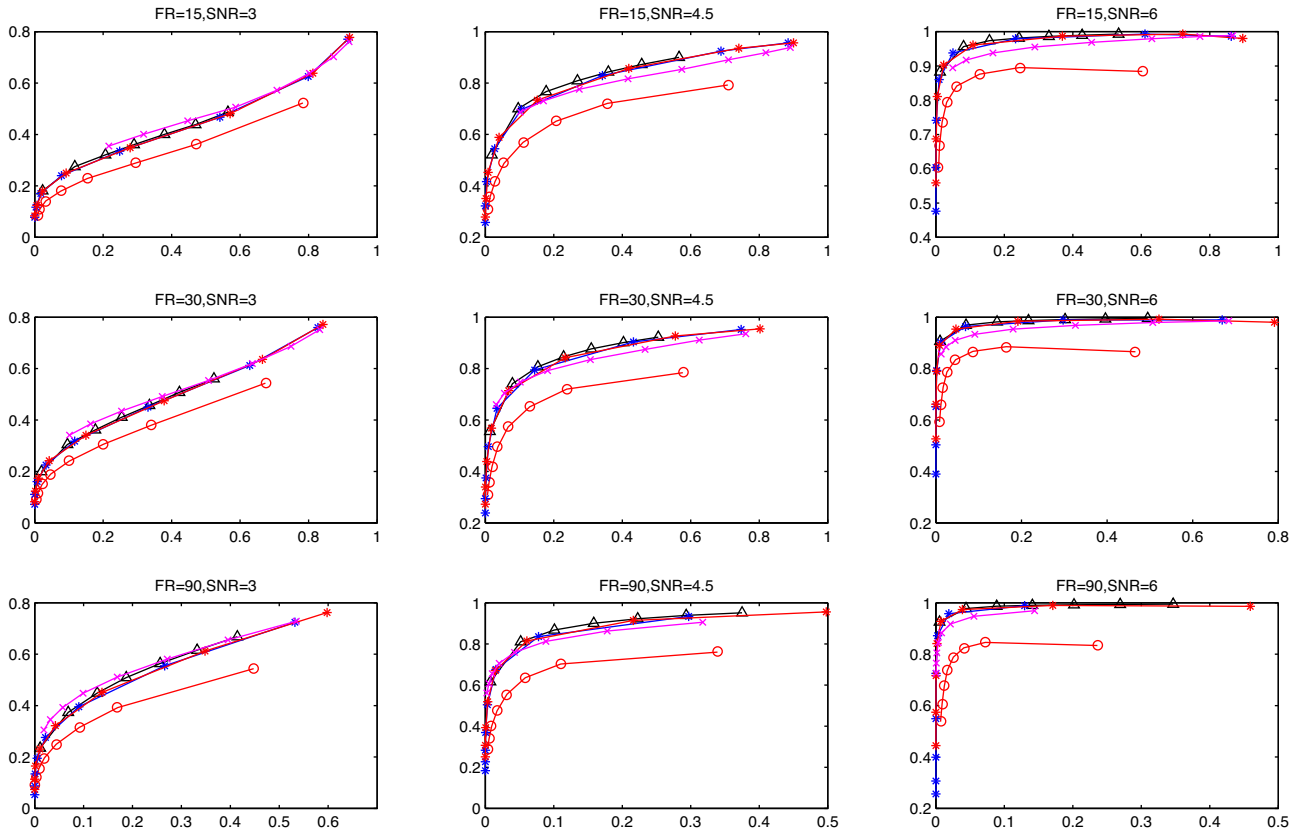

Fig. 4. ROC curves of five detectors under nine combinations of SNR and FR. ECPC: black triangles; CWD: red circles; AT: blue stars; MAD: red stars; NEO: magenta ×. Each curve is averaged from 100 random trials. (For interpretation of the references to color in this figure legend, the reader is referred to the web version of the article.)

changing during the recording. The whole simulated sequence was 3.5-min long. The firing rate was designed to be around 91 Hz at the very beginning and gradually decreased with a 15 Hz step for every 30-s. Finally the sequence ended with a firing rate of 1 Hz. The SNR is set to be high to make the FR the only parameter taken into consideration. Spike detection was performed every 30-s using four detectors, namely EC–PC, (continuous wavelet based detector) CWD, amplitude thresholding (AT), Median standard deviation (MAD) and NEO detectors. The threshold parameters of these detectors were fixed at the beginning (using the "optimal thresholds" given from ROC curves) and kept unchanged during the detection: EC–PC detector, probability threshold equals to 0.8, CWD, detection parameter equals to −0.1 with the "bior1.5" as the mother wavelet because as it is shown in Kim and Kim (2003) and Nenadic and Burdick (2005), the biorthogonal wavelets match the intrinsic structure of spike templates better than others. The number of scales is 8. In the AT, 3.5 times of data RMS value; MAD, 4 times of data STD; NEO 10 times of the mean of NEO output. For all the detectors, a spike is seen to be correctly detected if it is within 0.5 ms of the true arrival time given by ground truth data. The experiments were repeated 50 times to get statistical trends of FR change for each detector.

3.2.4. Experiment using simulated data – both FR and SNR changes

This experiment was designed to study the robustness of the detectors when the recording sequences have different FRs and different signal SNRs. Spike detection was performed under six firing rates ranging from 15 Hz to 90 Hz with a step of 15 Hz and eight SNRs from 2.5 to 6 with a step of 0.5. Under each of the total 6×8 combinations of FR/SNR, the experiments were performed 100 times and the averaged PFA vs. PD dots were to be plotted. The thresholds for each detector were fixed at the optimal values given previously.

3.2.5. Experiment using anesthetized rat data

We used real data from anesthetized rat to show the robustness of the EC–PC detector. Spike detection and simple firing rate estimation were performed every 5 min using 20 sec data. EC–PC detector and other four detectors, AT, MAD, NEO and CWD, were used as well. Three different thresholds are picked for each detector. EC–PC: probability threshold 0.5, 0.8 and 0.95. AT: amplitude threshold 3×RMS, 3.5×RMS and 4×RMS, MAD: amplitude threshold 3.5×STD, 4×STD and 4.5×STD, NEO: 8×Mean, 10×Mean and 12×Mean of NEO output, CWD: threshold parameter −0.15, −0.1, −0.05.

4. Results

4.1. Simulated data – ROC curves

Fig. 4 shows the ROC curves of five detectors under 9 combinations of SNRs/FRs. Each curve is generated from averaging 100 random trials. In ROC curves, *y*-axis is probability of detection (correctly detected spikes/total added spikes, PD), and *x*-axis is probability of false alarm (falsely detected spikes/total detected spikes, PFA). Fig. 5 is the ROC curve averaging from total 900 trials. It can be seen from the figures that no detection method can outperform the others in the entire situations. The results from CWD are worst because there are 30 spike templates with different shapes and width added in one sequence which cannot be well represented by single mother wavelet. We also get the "optimal thresholds" for the five detectors using the method explained in Section 3.2.1. The thresholds achieving the maximum number of

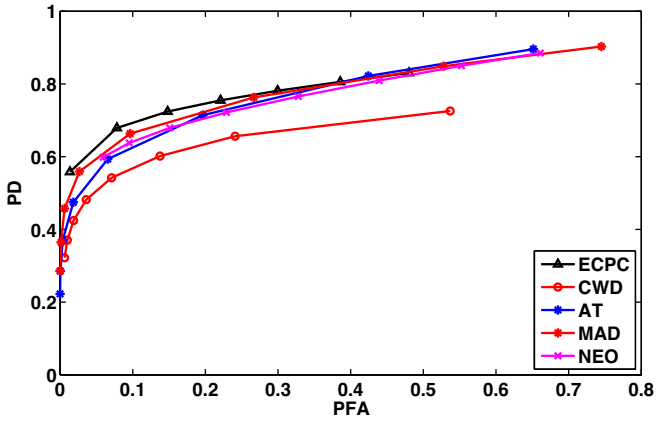

Fig. 5. ROC curves averaging from total 900 trials.

reasonable detection results are seen to be optimal and have been used in the rest experiments which are: EC–PC = 0.8, CWD = −0.1, AT = 3.5 × RMS, MAD = 4 × STD, NEO = 10.

4.2. Simultaneous recording data – SNR changes

Table 1 and 2 summarize the detection results of the EC–PC spike detector on simultaneous intracellular recording data when the probability threshold PTH is set at 0.8 and 0.9 respectively. In each table, the results are averaged from 100 trials and the standard deviations are shown in the brackets. The SNRs of the data are ranging from 6 to 3, leading to an increasing FN and a decreasing TP. Comparing the results under same SNR but different thresholds, the larger threshold gives worse TP but better FP. The unique advantage of the EC–PC detector is that given a probability threshold, the detection Precision (TP/(TP + FP)) is insensitive to the SNR and the value of Precision is around the value of probability threshold as shown in the PR columns. This point is further proved by the experimental results in Section 4.6.

4.3. Simulated data – FR changes

The estimated firing rates (detected spike number divided by 30-seconds) given by five detectors are plotted in Fig. 6. We have performed the spike detection for 50 times and the results were plotted in the figures with each gray curve from one random trial. The true firing rate was denoted as black solid line. The thresholds of each detector were fixed at the previously selected value. At the beginning, the firing rates of all the detectors showed some deviation from the true firing rate. Those of CWD, AT, MAD and NEO were smaller while those of EC–PC was a little bit larger. During 3.5 min long spike detection, EC–PC, CWD and MAD detectors followed the true FR curve and gave FR around 1 Hz in the end. However NEO and AT failed to follow the true firing rate curve in the end where they gave FR around 10 Hz much larger than the true value 1 Hz. They are not robust to the firing rate changes because they missed many spikes at the beginning of the sequence which indicated oversized thresholds but introduced many false alarms in the end indicating undersized threshold. The change of the FR causes both positive and negative errors for NEO and AT which cannot be compensated by optimizing the threshold parameters at the beginning of the recording. EC–PC and MAD performed better than CWD because FR of CWD began to be larger than true FR at 3 min though the maximum error was small.

4.4. Simulated data – both FR and SNR changes

The PFA versus PD dots is shown in Fig. 7 with each dot averaged from 100 random trials. The thresholds for each detector were fixed at the optimal values given previously. It can be seen clearly that under different FR/SNR situations, AT, MAD, CWD and NEO detector have PFA vs. PD dots dispersedly spreading over the PFA-PD space. This seemed normal because the recording conditions were quite different. However it reveals a common disadvantage of these detectors that the detection performance is non-robust to the neural recording conditions. The change of the recording condition could in many cases make the detection result move from its original location in PFA-PD space to a lower right dot which means the same detector with same threshold parameter gives a worse detection result (larger PFA but smaller PD) when condition changes. Unlike those detectors, the PFA vs. PD dots from EC–PC detector represented a “virtual line” in the figure. In most cases, when the recording condition changes, the PFA vs. PD dots move along the line, which means no matter the recording situations, once the threshold is fixed, the EC–PC detector obeys the trade-off of PFA and PD and detection results with both worse PFA and worse PD can rarely occur. Moreover, the prediction of Detection Precision can be also verified in this experiment. Since the probability threshold is set at 0.8, the Precision (1-PFA) should be around 0.8 which is centered at 0.78 in this experiment.

Table 1
Detection result of EC–PC detector when $P_{TH} = 0.8$.

SNR	P	TP	FP	FN	SE	PR
6.0	301	292.1 (1.9)	91.1 (19.3)	8.8 (1.9)	0.97 (0.0064)	0.76 (0.038)
5.5	301	290.8 (2.0)	91.7 (17.2)	10.1 (2.0)	0.96 (0.0069)	0.76 (0.034)
5.0	301	288.3 (2.6)	85.0 (19.9)	12.6 (2.6)	0.95 (0.0087)	0.77 (0.042)
4.5	301	283.4 (3.0)	80.2 (18.1)	17.5 (3.0)	0.94 (0.0101)	0.78 (0.038)
4.0	301	269.1 (5.5)	69.7 (12.3)	31.9 (5.5)	0.89 (0.0185)	0.79 (0.028)
3.5	301	241.7 (5.8)	62.5 (13.6)	59.2 (5.8)	0.80 (0.0194)	0.79 (0.034)
3.0	301	203.1 (9.0)	46.5 (14.1)	97.8 (9.1)	0.67 (0.0301)	0.81 (0.040)

Table 2
Detection result of EC–PC detector when $P_{TH} = 0.9$.

SNR	P	TP	FP	FN	SE	PR
6.0	301	292.0 (1.7)	38.8 (9.1)	8.9 (1.7)	0.97 (0.0060)	0.88 (0.0244)
5.5	301	290.2 (2.1)	38.6 (8.1)	10.8 (2.1)	0.96 (0.0072)	0.88 (0.0222)
5.0	301	285.7 (2.9)	36.3 (8.1)	15.2 (2.9)	0.94 (0.0099)	0.88 (0.0228)
4.5	301	277.0 (4.3)	33.7 (7.9)	23.9 (4.3)	0.92 (0.0145)	0.89 (0.0227)
4.0	301	258.0 (6.5)	28.9 (8.5)	43.0 (6.5)	0.85 (0.0217)	0.89 (0.0265)
3.5	301	225.6 (8.3)	23.1 (6.1)	75.4 (8.3)	0.74 (0.0279)	0.90 (0.0212)
3.0	301	183.2 (8.5)	18.3 (5.8)	117.8 (8.5)	0.60 (0.0283)	0.91 (0.02440)

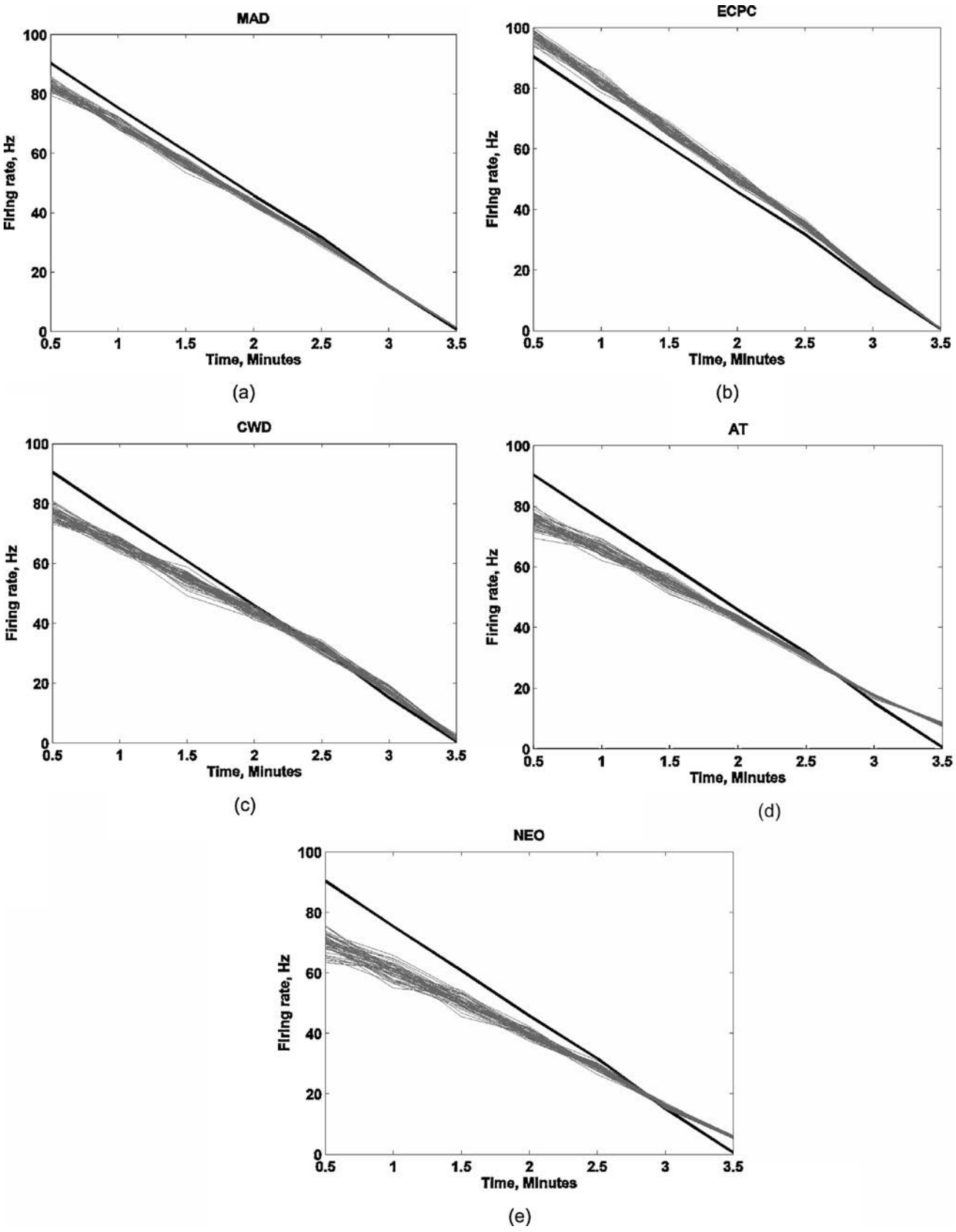

Fig. 6. The firing rate estimated by five detectors. Each gray curve denotes the result from one random trial. The true firing rate was denoted as black solid line.

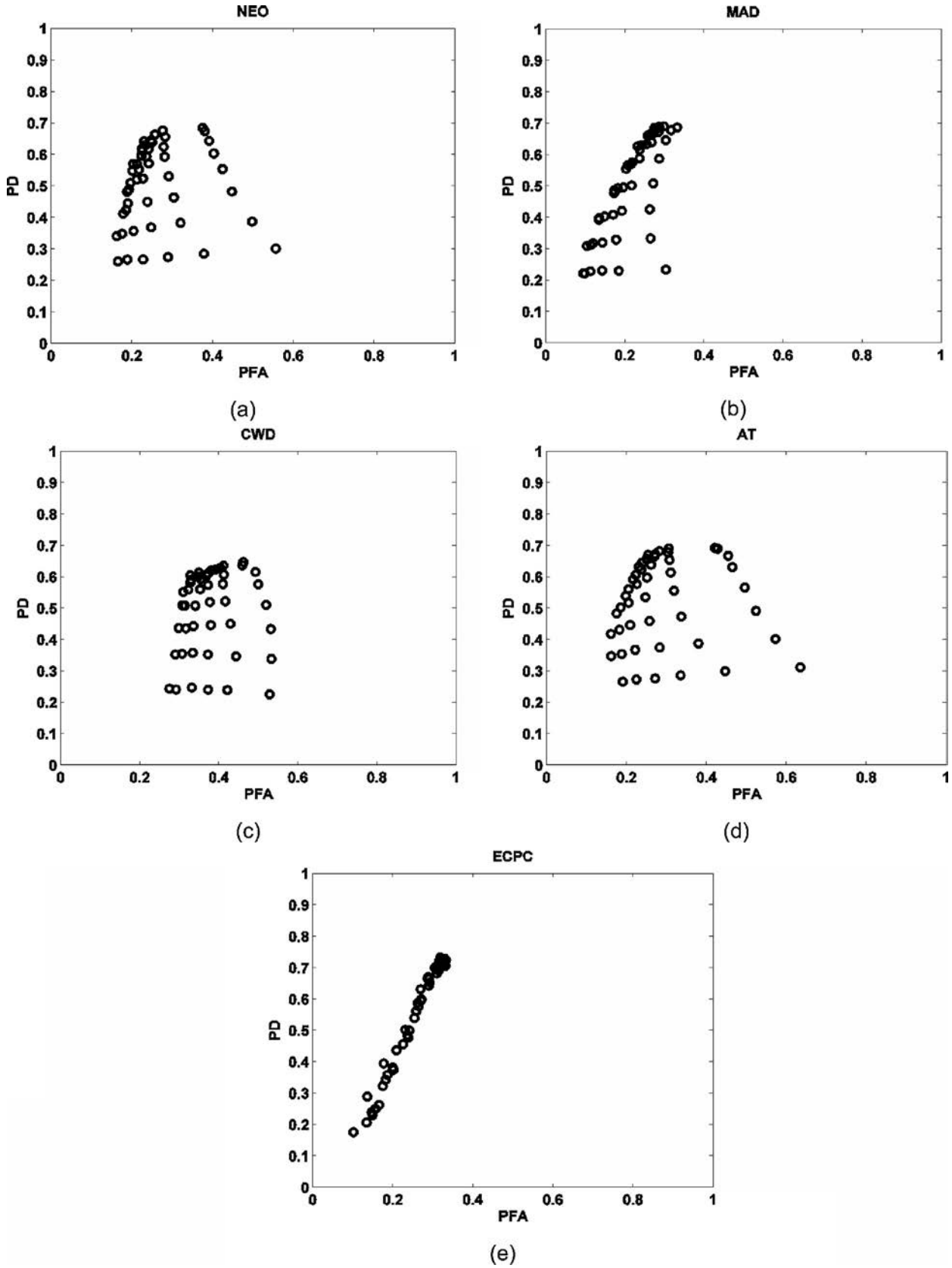

Fig. 7. Spike detection given by five detectors under six firing rates ranging from 15 Hz to 90 Hz with a step of 15 Hz and eight SNRs from 2.5 to 6 with a step of 0.5. Each dot represents the results under one combination of SNR and FR and is averaged from 100 random trials.

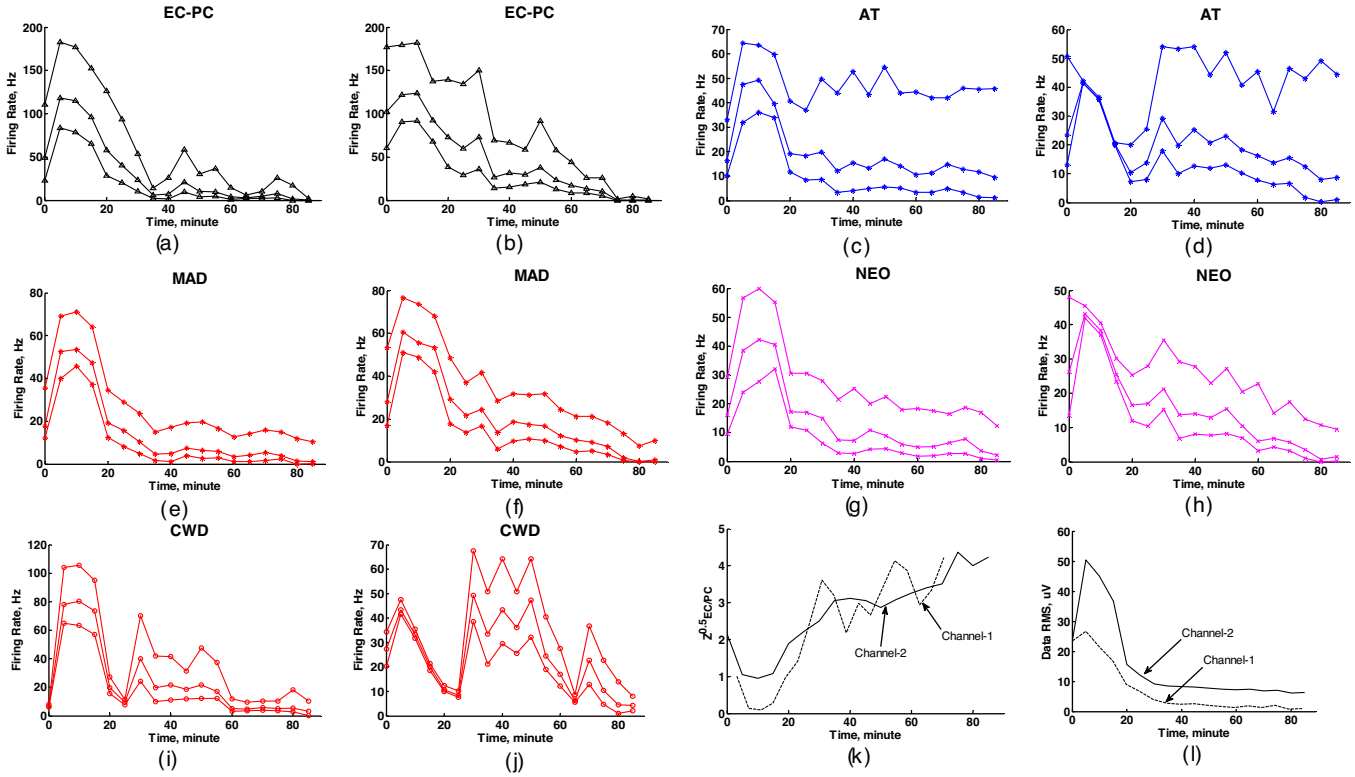

Fig. 8. (a)(c)(e)(g)(i) Estimated firing rate vs. time in channel-1, using EC–PC, AT, MAD,NEO and CWD detector respectively. Three curves in each figure are the results under three different thresholds. From upper to lower, for EC–PC: probability threshold 0.5, 0.8 and 0.95; for AT: amplitude threshold 3×RMS, 3.5×RMS and 4×RMS; for MAD: amplitude threshold 3.5×STD, 4×STD and 4.5×STD; for NEO: 8×Mean, 10×Mean and 12×RMS of NEO output; for CWD: threshold parameter −0.15, −0.1 and −0.05. (b)(d)(f)(h)(j) Estimated firing rate vs. time in channel-2 using the above detectors. (k) EC–PC crossing points and (l) data RMS.

4.5. Experiment using anesthetized rate data

Fig. 8(a)–(j) shows the firing rate vs. time curves from five detectors. Fig. 8(a)(c)(e)(g)(i) plots the results of channel-1 and Fig. 8(b)(d)(f)(h)(j) plot the results of channel-2. Fig. 8(l) shows the RMS value of the bandpass filtered data at 300 Hz–5 kHz, where the initial value is 25–50 V. For each detector, the thresholds were selected as: EC–PC = 0.5, 0.8, 0.95; AT = 3×RMS, 3.5×RMS, 4×RMS; MAD = 3.5×STD, 4×STD, 4.5×STD; NEO = 8, 10, 12 and CWD = −0.15, −0.1, −0.05. A robust spike detector should achieve the following detection results in this in-vivo experiment. First, since the neurons are dying over time, the overall trend of the firing rate should be decreasing. Second, at the end of the recording, there should be no spikes detected. For AT, NEO and CWD methods, even the optimal thresholds given in previous section are selected, the firing rate (middle curves) either not decrease to zero at the end of the recording (Fig. 8(c)(d)(g)(h)(i)(j)) or shows a weird trend (Fig. 8(j)).

When slightly change the threshold parameter, the results can be even worse. For AT, when the threshold changed from 3.5×RMS to 3×RMS, it gives wrong FR trend (upper traces) in both channels. For MAD with threshold changed from 4×STD to 3.5×STD, NEO with threshold changed from 10 to 8 and CWD with threshold changed from −0.1 to −0.15, the firing rates showed non-neglectable values (>10 Hz) at the end of the recording. These detectors maybe perform well under good threshold choices; however, since the optimal threshold is not accessible in the most cases, the high sensitivity to their threshold level could give these detectors non-robust manners in the real experiment. In contrast, for EC–PC detector using thresholds from as large as 0.95 to as small as 0.5, the firing rates perfectly followed decreasing trend and went to near zero at the end of the recording. This is because as the brain dies, the RMS value of the recorded data decrease but the EC/PC crossing point as plotted in Fig. 8(k) shows an increasing trend over time which leads to less detected events. This experiment proves ECPC detector a good candidate for robust and unsupervised spike detection.

4.6. Statistical significance of the EC–PC detector

The predicted Precision by (8) versus true Precision curves are plotted in Fig. 9(a)–(c). The x-axis is the probability threshold, also predicted Precision, varying from 0.5 to 0.99. The y-axis is the true Precision, obtained by comparing the detection results with ground truth. The result from each sequence is denoted by a gray curve while the mean trend and standard deviation are denoted by black curve with error bar. When noise has a $1/f^{1.5}$ power spectrum (Fig. 9(a)), the mean predicted detection Precision perfectly matches the ground truth indicating α have a value close to 1. Because most of the neural noise spectrum exhibits a $1/f^{1.5}$ dependency (Yang et al., 2009), the prediction is valid in most cases. When noise has a $1/f$ power spectrum (Fig. 9(b)), there is slight deviation from the line $y = x$. Even when noise is white (Fig. 9(c)), which may not appear in animal data, the mean prediction curve is still within an acceptable range. Fig. 9(d) shows the statistics of α under different noise, which centers at 0.96, 1.26 and 2.02 with standard deviation 0.17, 0.40 and 0.45 respectively. Large α leads to underestimated true Precision, which explains the deviation from prediction in Fig. 9(b)–(c).

We have shown through the simulation that within a wide range of firing rates and SNRs, predicted Precision vs. true Precision curves give clear trends along the line $y = x$ with a few outliers. These simulation results prove that the probability threshold can reliably predict the detection Precision. Thus for the first time, we are able to set detection threshold by means of closely connecting the threshold with expected Precision of spike assemble. For example, some experimentalists may set the probability threshold at 0.5 in order to get more spikes while keeping the confidence that nearly half of

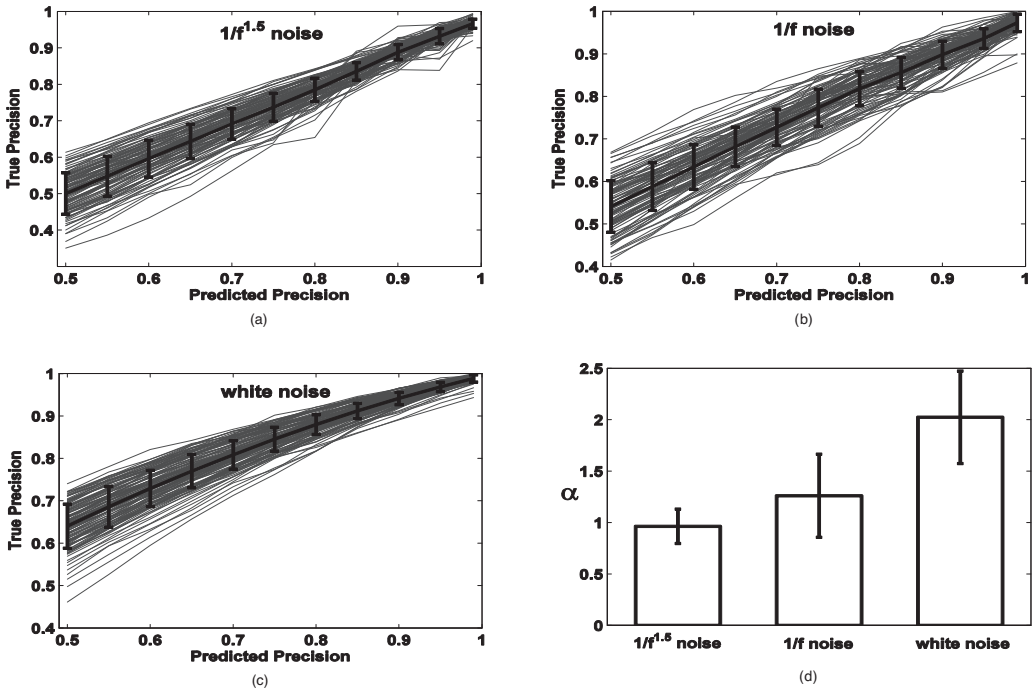

Fig. 9. Simulation results for the validation of Eq. (8). (a)–(c) are predicted Precision vs. true Precision curves. The *X*-axis is probability threshold, also the predicted Precision, changing from 0.5 to 0.99, and the *Y*-axis is the true Precision obtained by comparing the detection results with the ground truth data. Each gray curve denotes one sequence's result while total 121 synthesized sequences are used covering a wide range of firing rate (15–90 Hz) and SNR (3–5). The black curve shows the averaged trend with standard deviation error bars. The background noise added in the sequences is $1/f^{1.5}$ noise (a), $1/f$ noise (b) and white noise (c) respectively. (d) Shows the statistics of α in Eq. (8) given three kinds of noise.

the spikes are true. And some others may set probability threshold at 0.99 to make sure that almost all the detected spikes are true. Tradeoff between more spikes and more false alarms can be explicitly made given probability threshold. This property is useful for online spike detection where robust and consistent spike information is needed to support subsequent processing.

5. Hardware implementation

We have implemented our proposed EC–PC spike detection algorithm into a 16-channel neural signal processing ASIC chip. A block diagram description of the implemented prototype is given in Fig. 10, where blocks enclosed in the yellow-line envelope have been integrated on-chip. After being recorded, digitized, and encoded, raw neural data time-multiplexed for 16 channels are fed into the neural signal processing system with an effective data rate up to 10.24 Mbps. Input data are decoded first, and low-pass filtered with a corner frequency at 250 Hz to obtain low-frequency field potentials. In another pathway, neural data are band-pass filtered with default corner frequencies at 300 Hz and 8 kHz to band-limit components where spikes reside. To handle a variety of noise profiles and spike characteristics, the band-pass filter has

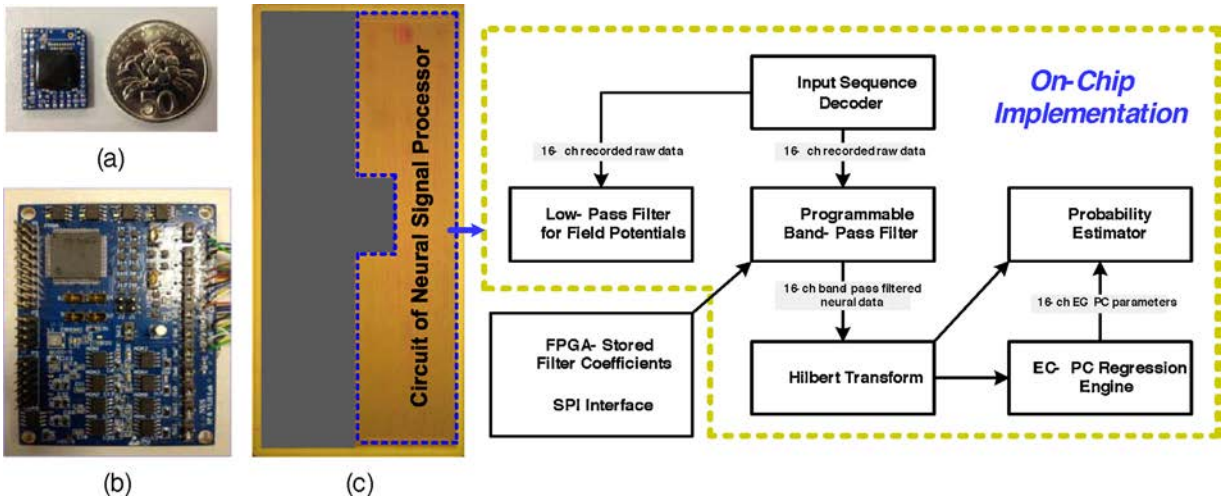

Fig. 10. Hardware system of the neural signal processing IC. (a) The mounting PCB of the designed chip. (b) The evaluation board of the prototyping system. (c) The die photo of the designed chip. Enclosed region are the block diagram of the neural signal processing system. (For interpretation of the references to color in the text, the reader is referred to the web version of the article.)

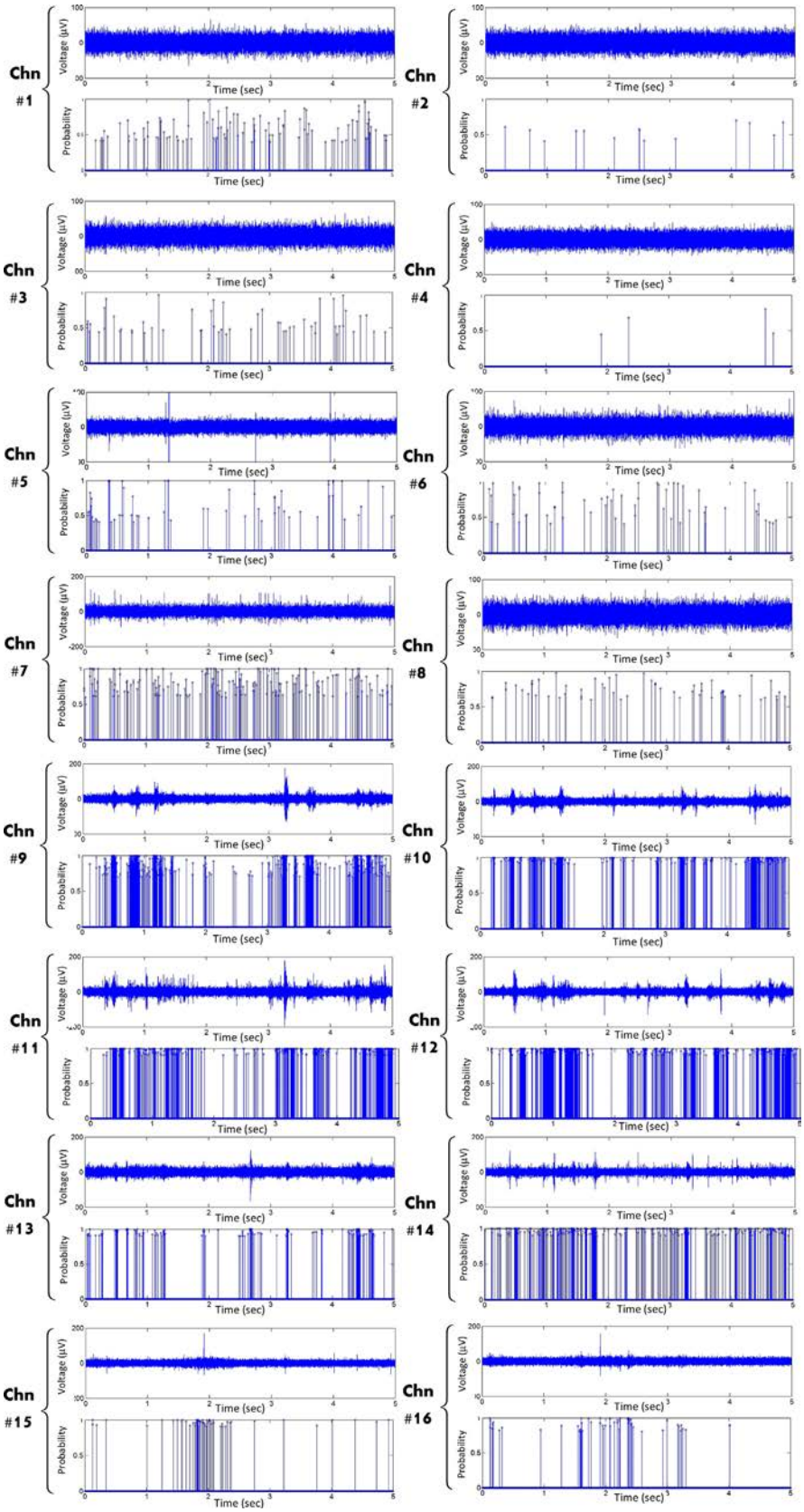

Fig. 11. 16-Channel simultaneous outputs of the ASIC. For each channel, the upper is the band-pass filtered neural data and the lower is the generated probability map.

25 programmable coefficients, and thus can be configured to work at different corner frequencies with at least 60 dB stop-band attenuation and less than 0.1 dB in-band ripples.

The Hilbert transform and the EC–PC regression engine, as a whole, are to estimate neural data distribution and perform EC–PC decomposition. A periodic training mechanism is incorporated in the design of the regression engine to deal with the non-stationary and non-Gaussian characteristics of neural data, which is fully autonomous and executing in real-time with low latency. Specifically, the regression engine can report the EC–PC parameters of 16 channels within 0.8 ms, a negligible delay for neural signal processing applications. At last, a probability estimator is employed to calculate the spiking probability maps based on the trained EC–PC parameters and the neural data represented in Hilbert space. A winner-take-all strategy is implemented inside the probability estimator, where the neural data sample with the highest probability value in a 64-point sliding window is identified. By outputting the probability scores and the timestamps associated with the identified data points, a 64× data rate reduction from 10.24 Mbps to 160 kbps is achieved, facilitating wireless data transmission.

In this implementation, hardware-sharing is exploited extensively to reduce computational complexity and storage cost. For example, circuit blocks including the low-pass filter, the band-pass filter, the Hilbert transform module, and the probability estimator are all time-interleaved to support the processing of 16-ch time-multiplexed neural data. As another contribution toward low storage cost, each register array for approximating neural data distributions is allocated to 4 channels in sequence, thus achieving a 4× reduction in required storage from 6 kb to 1.5 kb. The chip occupies a core area of 0.41 mm^2 per channel in a 0.13 μm process and consumes a peak power of 85 μW per channel from a 1.2 V supply voltage when the training for all 16 channels are performed simultaneously. In summary, by leveraging the optimization techniques introduced above, the dedicated neural signal processing circuit has realized a low-power and area-efficient design, making it suitable as wireless and implantable neural recording and processing devices.

As shown in Fig. 10, the chip is packaged in a small printed circuit board (PCB) with a size of 1.9 cm × 1.5 cm, connected to a NeuroNexus microelectrode array. A credit card size board (5.4 cm × 7.5 cm) including a FPGA, SRAMs, level shifters, power managements and interfaces is used as an evaluation board to provide a complete testing benchtop that requires only one USB cable as power and data link. A demonstration of the prototyping system to output spike signals and probability maps for 16 channels is shown in Fig. 11, where the 16 testing sequences cover a wide range of spiking activities with different SNRs and firing-rates. In each sub-figure, the probability map gives more dense bins when there are more visually differentiable spikes, as expected.

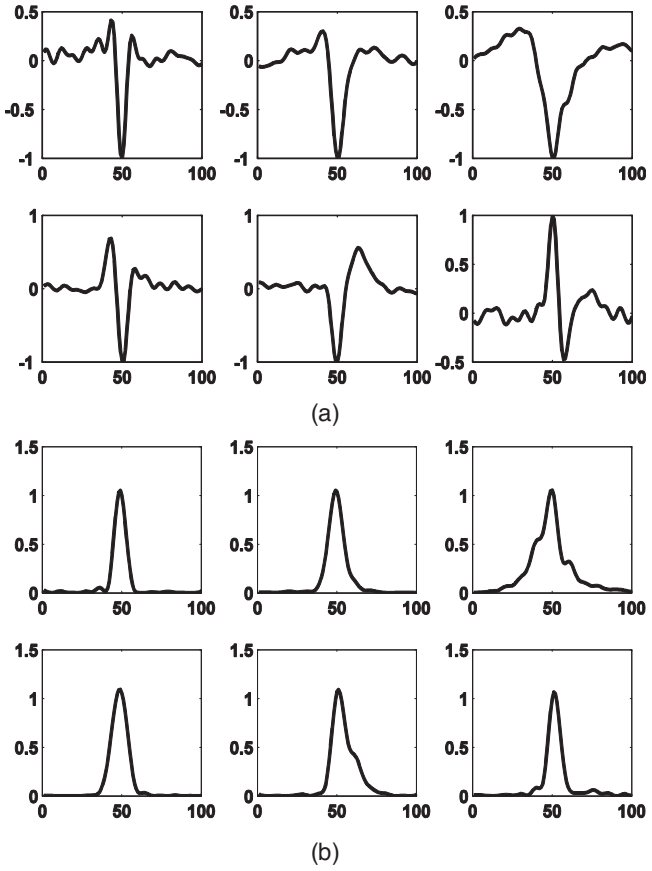

Fig. 12. (a) Six spike templates extracted from in vivo data with different shape and width. They are plotted in 2.5 ms windows and are normalized to their amplitude. (b) Their corresponding Hilbert spikes obtained from using (2) and (3). The shapes can be approximated by triangles.

6. Discussion

Despite many spike detection algorithms reported in the literature, how to set the threshold remains an unresolved technical challenge. In fact the choice of threshold can majorly influence information decoding. In BCI experiments, researchers usually empirically select a subset of channels and manually set detection threshold. Offline data analysis suggests manually adjusting the threshold over time and over each individual channel can improve decoding accuracy. In online applications, it is ambitious to manually adjust threshold in an optimal manner. Thus we have come up with this EC–PC algorithm to automatically set detection threshold of each channel. We have tried our algorithms on monkey data recorded from behavior experiments over three days, where we can see substantially improved decoding accuracy increasing from 45% to 93% by using a same decoder. The behavior experiments are still on-going and the results will be reported in future publications.

A second motivation of our algorithm is to compress the recorded data and make the data rate manageable for a wireless transceiver. It takes about 10 mA in total to transmit 1 Mbps data using a state-of-the-art commercial wireless system. Further increased data rate somehow is not as realistic for wireless transmission due to the constraints from power, size, and reliability. As a result, it requires an appropriate signal processing algorithm integrated on-chip that can compress the data and the signal processing hardware itself should be low power and small size. In this paper, we have demonstrated our algorithm can be integrated on-chip with a peak power consumption of 85 μW per channel. We are working on further power reduction by optimizing the algorithm, using deep sub-threshold circuit design techniques, and developing custom low-power on-chip memory. Simulation results suggest that we can push the current signal processing hardware to 2 μW per channel eventually. Once this is done, it would enable some new neural interface circuits and experiments. We will report the results when our new chip has been tested. In summary, we envision that the EC–PC algorithm and hardware can be used in real-time neural recording experiments and improve decoding performance.

Acknowledgements

The authors would like to acknowledge the funding support 622 by A*STAR PSF Grant R-263-000-699-305, NUS YIA Grant 623 R-263-000-A29-133 and MOE R-263-000-A47-112.

Appendix A. Neural data distribution

To study both signals and noise in highpass filtered neural data, we refer to Central Limit Theorem (CLT).

Theorem 2. *Let X_i, $i = 1, 2, 3, \ldots, K$ be a sequence of independent random variables. Suppose that each Xi has a finite expected value $E[X_i] = \mu_i$ and a finite variance $E[(X_i - \mu_i)^2] = \sigma_i^2$. If for some $\delta > 0$, the expected values $E[|X_i|^{2+2\delta}]$ are finite and the Lyapunov's condition*

$$\lim_{K\to\infty} \frac{1}{\left(\sum_{i=1}^{K} {\sigma_i}^2\right)^{1+\delta}} \sum_{i=1}^{K} E[|X_i - \mu_i|^{2+2\delta}] = 0$$

is satisfied, then the convergence to Gaussian holds, i.e. $\sum_{i=1}^{K} X_i$ follows a Gaussian distribution with mean $\sum_{i=1}^{K} \mu_i$ and variance $\sum_{i=1}^{K} {\sigma_i}^2$.

Treating voltage fluctuation induced by individual neuronal source as a random variable (spike, synapse), the recorded data are the sum of many random variables with additional Gaussian noise by electrode interface and electronics. There are two issues regarding applying Lyapunov's condition here. First, only a moderate number of neurons located in a proximity region (e.g. a few hundred μm) of the recording site could be treated as the pool for Lyapunov's condition, making the large number hypothesis questionable. Second, the strength of pairwise synchronization of neural activities is inversely proportional to the distance between the neurons (Koch, 2004), implying that the random variables to be summed over are not completely independent. Due to the violations of Lyapunov's conditions, recorded neural data can be modeled as a mixture of Gaussian distribution by noise (Yu et al., 2001) and small amplitude activities from distant neurons (>100 μm) (Buzsaki et al., 2012) and a second distribution by detectable spikes.

As we mentioned in Section 2, for low SNR recordings, e.g., no visually detectable spikes, the probability density function $f(Z)$ is contributed by just noise and background activities, following exponential distribution as (3). For moderate and high SNR recordings, $f(Z)$ noticeable deviates from a straight line. To quantitatively investigate this deviation, we examine the following equations:

$$N \propto r^3 \tag{9}$$

$$V_M \propto 1/r^x, 1 \le x \le 2 \tag{10}$$

$$Z_M \approx V_M^2 \tag{11}$$

Eq. (9) simply shows the case when an electrode is located at the center of a sphere with radius r. Then the number of neurons N enclosed inside of this sphere is proportional to r^3, assuming a homogeneous neuron spatial distribution. Eq. (10) shows that V_M, the amplitude of spikes fired by individual neurons, decays inversely proportional to r^x where x is within 1–2. Eqs. (11) and (2) show that the peak power of the spike after Hilbert transform is approximately equal to the square of its original voltage amplitude V_M because the imaginary part of V_{st} in (1) is nearly zero at the spike peak. Given the above three equations, the density function of the number of neurons with respect to spike peak power Z_M, can be derived

$$\rho(Z_M) \propto Z_M^{-((3+2x)/2x)}, \quad 1 \le x \le 2 \tag{12}$$

To see how each spike contributes to $f(Z)$, we plot six spike templates with different width and shapes and their corresponding waveforms after Hilbert transform, as shown in Fig. 12(a) and (b) respectively. The spike templates are extracted from in vivo data and normalized to their amplitude. All the templates are plotted in a 2.5 ms window. Fig. 12(b) shows that regardless of the original spike waveforms, their shapes after Hilbert transform (according to (2) and (3)) can be approximately modeled by triangles. Spikes' contribute to $f(Z)$ now can be directly derived based on two facts: (1) the contribution to $f(Z)$ is from all the Hilbert spikes with peak Z_M larger than Z. So the overall spike contribution is a summation. (2) The amount of contribution can be represented by the number of data points falling in a bin centered at Z. When the Hilbert spike shape is modeled by a triangle, the number of data points in the bin is proportional to the Hilbert spike width and inversely proportional to the Hilbert spike peak Z_M. An illustration is shown in Fig. 13, for calculating $f(Z)$, we count the number of spike points in the bin $(Z - \Delta Z/2, Z + \Delta Z/2)$. Spike 2 contributes to $f(Z)$ more than spike 3 while spike 1 does not make any contribution. Therefore the second distribution $f_d(Z)$, caused by spikes, is a polynomial function as

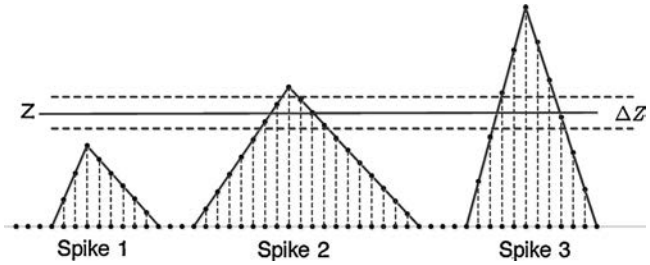

Fig. 13. Illustration of Hilbert spikes' contribution to $f(Z)$. For calculating $f(Z)$, the number of spike points in the bin $(Z - \Delta Z/2, Z + \Delta Z/2)$ need to be counted. The contribution to $f(Z)$ is proportional to the Hilbert spike width and inversely proportional to the Hilbert spike amplitude. As an example, spike 2 contributes to $f(Z)$ more than spike 3 because spike 2 has larger width and smaller amplitude. While does not contribute to $f(Z)$ because its peak is smaller than Z.

$$f_d(Z) \approx \int_Z^{+\infty} \rho(Z_M) \frac{\Delta Z W}{Z_M} dZ_M \propto Z^{-((3+2x)/2x)} \tag{13}$$

where W is the averaged Hilbert spike width in terms of sample number.

Appendix B. Proof of Theorem 1

The detailed mathematical proof is as follows. When a probability threshold P_{TH} is determined, according to (5), there will be a unique value of signal power, denoted by Z_{TH} satisfying

$$P_{TH} = p(Z_{TH}) = \frac{\tilde{f}_d(Z_{TH})}{\tilde{f}_d(Z_{TH}) + \tilde{f}_n(Z_{TH})} \tag{14}$$

Assume there are N_{cd} true spikes and N_{fd} false spikes in the total N_d detected spikes. Consider the contribution from true spikes, (12) can be expanded using (4) as

$$P_{TH} = p(Z_{TH}) \approx \frac{\Delta Z W \sum_{Z_{Mi} \ge Z_{TH}} (1/Z_{Mi})}{\Delta Z W \sum_{Z_{Mi} \ge Z_{TH}} (1/Z_{Mi}) + n\tilde{f}_n(Z_{TH})}$$

$$= \frac{\Delta Z W (1/\overline{Z}) N_{cd}}{\Delta Z W (1/\overline{Z}) N_{cd} + n\tilde{f}_n(Z_{TH})}$$

where Z_{Mi} denotes the amplitude of each true spikes after Hilbert transform, n is total number of data points and $\overline{Z}$ is the averaged true Hilbert spike amplitude satisfying

$$\frac{1}{\overline{Z}} = \frac{1}{N_{spike}} \left(\frac{1}{Z_1} + \frac{1}{Z_2} + \cdots + \frac{1}{Z_{N_{cd}}} \right)$$

Noise pdf $\tilde{f}_n$ can be expanded in a similar manner, thus

$$P_{TH} = p(Z_{TH}) = \frac{(W/\overline{Z}) N_{cd}}{(W/\overline{Z}) N_{cd} + (W_n/\overline{Z}_n) N_{fd}}$$

with W_N and $\overline{Z}_n$ being averaged false spike width and amplitude. However W_N and $\overline{Z}_n$ only have a mathematical meaning because

false spikes do not contribute to $\tilde{f}_n(Z_{TH})$ as consistent and determinant as true spikes do. To simplify the analysis, (5) can be arranged as

$$P_{TH} = \frac{N_{cd}}{N_{cd} + \alpha N_{fd}}$$

when α is close to one, the *Precision* can be approximated to the numeric value of probability threshold P_{TH} as

$$\text{Precision} \approx \frac{N_{cd}}{N_{cd} + \alpha N_{fd}} = P_{TH}$$

and proof id complete.

References

Belitski A, Gretton A, Magri C, Murayama Y, Montemurro MA, Logothetis NK, et al. Low-frequency local field potentials and spikes in primary visual cortex convey independent visual information. J Neurosci 2008];28(22):5696–709.

Buzsaki G. Rhythms of the brain. USA: Oxford University Press; 2006].

Buzsaki GA, Anastassiou CA, Koch C. The origin of extracellular fields and currents – EEG, ECoG, LFP and spikes. Nat Rev Neurosci 2012];13(June (6)): 407–20.

Chandra R, Optican L. Detection, classification, and superposition resolution of action potentials in multiunit single-channel recordings by an on-line real-time neural network. IEEE Trans Biomed Eng 1997];44(5):403–12.

Choi JH, Jung HK, Kim T. A new action potential detector using the MTEO and its effects on spike sorting systems at low signal-to-noise ratios. IEEE Trans Biomed Eng 2006];53(4):738–46.

Fawcett T. An introduction to ROC analysis. Pattern Recogn Lett 2006];27(8):861–74.

Gerstner W, Kreiter AK, Markram H, Herz AV. Neural codes: firing rates and beyond. Proc Natl Acad Sci U S A 1997];94(November (24)):12740–1.

Gibson S, Chandler R, Karkare V, Markovic D, Judy J. An efficiency comparison of analog and digital spike detection. In: 4th international IEEE/EMBS conference on neural engineering, 2009. NER '09; 2009]. p. 423–8.

Gibson S, Judy J, Markovic D. Technology-aware algorithm design for neural spike detection, feature extraction, and dimensionality reduction. IEEE Trans Neural Syst Rehabil Eng 2010];18(October (5)):469–78.

Goodall E, Horch K. Separation of action potentials in multiunit intrafascicular recordings. IEEE Trans Biomed Eng 1992];39(3):289–95.

Gosselin B, Sawan M. An ultra low-power CMOS automatic action potential detector. IEEE Trans Neural Syst Rehabil Eng 2009];17(4):346–53.

Gozani SN, Miller JP. Optimal discrimination and classification of neuronal action potential waveforms from multiunit, multichannel recordings using software-based linear filters. IEEE Eng Med Biol 1994];41(April (4)):358–72.

Harris KD, Henze DA, Csicsvari J, Hirase H, Buzsáki G. Accuracy of tetrode spike separation as determined by simultaneous intracellular and extracellular measurements. J Neurophysiol 2000];84(July (1)):401–14.

Harrison RR. A low-power integrated circuit for adaptive detection of action potentials in noisy signals. In: Proceedings of the annual international conference of the IEEE engineering in medicine and biology, vol. 4; 2003]. p. 3325–8.

Henze DA, Borhegyi Z, Csicsvari J, Mamiya A, Harris KD, Harris KD, et al. Intracellular features predicted by extracellular recordings in the hippocampus in vivo. J Neurophysiol 2000]:390–400.

Kaneko H, Suzuki S, Okada J, Akamatsu M. Multineuronal spike classification based on multisite electrode recording, whole-waveform analysis, and hierarchical clustering. IEEE Trans Biomed Eng 1999];46(3):280–90.

Kim KH, Kim SJ. Neural spike sorting under nearly 0-db signal-to-noise ratio using nonlinear energy operator and artificial neural-network classifier. IEEE Trans Biomed Eng 2000];47(10):1406–11.

Kim KH, Kim SJ. A wavelet-based method for action potential detection from extracellular neural signal recording with low signal-to-noise ratio. IEEE Trans Biomed Eng 2003];50(8):999–1011.

Kim S, McNames J. Automatic spike detection based on adaptive template matching for extracellular neural recordings. J Neurosci Methods 2007];165(2): 165–74.

Koch C. The quest for consciousness: a neurobiological approach. Roberts & Company Publishers; 2004], http://www.amazon.com/Quest-Consciousness-Neurobiological-Approach/dp/0974707708

Lewicki MS. A review of methods for spike sorting: the detection and classification of neural action potentials. Netw Comput Neural Syst 1998];9(4):53–78.

Maragos P, Kaiser J, Quatieri T. On amplitude and frequency demodulation using energy operators. IEEE Trans Signal Process 1993];41(4):1532–50.

Mtetwa N, Smith LS. Smoothing and thresholding in neuronal spike detection. 14th annual computational neuroscience meeting (CNS 05), Madison, WI, July 17–21, 2005. Neurocomputing 2006];69(June (10–12)):1366–70.

Mukhopadhyay S, Ray GC. A new interpretation of nonlinear energy operator and its efficacy in spike detection. IEEE Trans Biomed Eng 1998];45(2):180–7.

Nenadic Z, Burdick J. Spike detection using the continuous wavelet transform. IEEE Trans Biomed Eng 2005];52(1):74–87.

Obeid I. Comparison of spike detectors based on simultaneous intracellular and extracellular recordings. In: 3rd international IEEE/EMBS conference on neural engineering, 2007. CNE '07; 2007]. p. 410–3.

Quiroga RQ, Nadasdy Z, Ben-Shaul Y. Unsupervised spike detection and sorting with wavelets and superparamagnetic clustering. Neural Comput 2004];16(8):1661–87.

Semmaoui H, Drolet J, Lakhssassi A, Sawan M. Setting adaptive spike detection threshold for smoothed TEO based on robust statistics theory. IEEE Trans Biomed Eng 2012];59(2):474–82.

Shahid S, Walker J, Smith L. A new spike detection algorithm for extracellular neural recordings. IEEE Trans Biomed Eng 2010];57(4):853–66.

Shalchyan V, Jensen W, Farina D. Spike detection and clustering with unsupervised wavelet optimization in extracellular neural recordings. IEEE Trans Biomed Eng 2012];59(9):2576–85.

Yang Z, Liu W, Keshtkaran MR, Zhou Y, Xu J, Pikov V, et al. A new ECPC threshold estimation method for in vivo neural spike detection. J Neural Eng 2012];9(4):046017.

Yang Z, Zhao Q, Keefer E, Liu W. Noise characterization, modeling, and reduction for in vivo neural recording. In: Bengio Y, Schuurmans D, Lafferty J, Williams CKI, Culotta A, editors. Advances in neural information processing systems, vol. 22; 2009]. p. 2160–8.

Yu S, Yang H, Nakahara H, Santos GS, Nikolić D, Plenz D. Higher-order interactions characterized in cortical activity. J Neurosci 2011;31(November (48)):17514–26.

Zouridakis G, Tam DC. Multi-unit spike discrimination using wavelet transforms. Comput Biol Med 1997];27(1):9–18.